Journal of Materials Chemistry A

ROYAL SOCIETY OF CHEMISTRY

PAPER

View Article Online
View Journal | View Issue

Cite this: J. Mater. Chem. A, 2025, 13, 7488

Exploring structural and electronic properties of transition metal carbides (T = Ti, V, Mo, & W) as efficient catalysts for overall water splitting with the DFT study†

Tata Sanjay Kanna Sharma, ‡[a] Jayasmita Jana,‡[a] Beena Mol Babu,[a] Mohamed A. Ghanem, [b] K. C. Bhamu, [a] K. S. S. V. Prasad Reddy, [a] Kuo-Yuan Hwa,[c] Sung Gu Kang,[a] Jin Suk Chung, [a] Seung Hyun Hur *[a] and Won Mook Choi *[a]

Earth abundant transition metal carbides (TMCs), including titanium carbide (TiC), vanadium carbide (VC), molybdenum carbide (MoC), and tungsten carbide (WC), are considered promising materials to substitute expensive novel metal Pt- and Ir-based catalysts since they can demonstrate exceptional electrocatalytic performance towards overall water splitting due to their unique electronic and structural properties. Herein, this work demonstrated the facile synthesis of different TMCs and investigated their electrocatalytic activities for alkaline water electrolysis. The prepared WC exhibited superior electrocatalytic activity towards the hydrogen evolution reaction (η_{100} = 295 mV) and MoC showed excellent electrocatalytic activity towards the oxygen evolution reaction (η_{100} = 373 mV), which are comparable to those of commercial Pt/C and IrO_2 catalysts, respectively. The mechanistic investigation indicated that the optimized orbital hybridization of TMCs balances the adsorption and desorption of reaction intermediates resulting in variations in their efficiency. In addition, the theoretical DFT study demonstrated the oxidative response of the prepared WC and MoC surfaces for overall water splitting by identifying the chemisorbed oxygen atoms.

Received 4th September 2024
Accepted 27th January 2025

DOI: 10.1039/d4ta06264g

rsc.li/materials-a

Introduction

Environmental contamination and resource scarcity have precipitated an energy crisis, catalyzing the advancement of clean-energy technologies as alternatives to fossil fuel consumption. It is pivotal in renewable energy endeavors to develop efficient electrocatalysts with considerations such as high performance, durability, cost-effectiveness, and efficacy in conversion and storage serving as critical factors.[1] Electrocatalysts exhibit versatility across applications such as water splitting, metal–air batteries, fuel cells, and processes involving the hydrogen evolution reaction (HER), oxygen evolution reaction (OER), oxygen reduction reaction (ORR), CO_2 conversion, and urea production by reducing the thermodynamic barrier of individual steps of multi-step reactions.[2] Here noble metals and their oxides, including platinum (Pt), ruthenium oxide (RuO_2), and iridium oxide (IrO_2), play a dominant role in advanced electrocatalyst applications. However, these noble metals show critical disadvantages, such as high cost, scarcity, and degradation, which can hinder their widespread application, especially in large-scale industrial processes. These limitations have driven research efforts toward developing alternative electrocatalysts that are more cost-effective, abundant, stable, and efficient for various electrochemical processes.[3] To address this, researchers have focused on transition metal-based materials, such as nitrides, phosphates, sulfides, and oxides, particularly in two-dimensional (2D) forms. However, they often require co-catalysts or bimetallic systems to achieve higher efficiencies,[4–7] along with complex synthetic routes,[8–10] with respect to conventional 2D materials such as graphene and MXene where their multiple layers with certain defects provide high tensile strength, mechanical durability, electronic mobility, and thermal conductivity. In this context, earth-abundant transition metal carbides (TMCs) have demonstrated significant efficiency due to their crystalline parameters, which enable tuning of electronic properties, as well as their high mechanical and

[a]School of Chemical Engineering, University of Ulsan, Daehak-ro 93, Nam-gu, Ulsan 44160, Republic of Korea. E-mail: shhur@ulsan.ac.kr; wmchoi98@ulsan.ac.kr

[b]Chemistry Department, College of Science, King Saud University, Riyadh 11451, Saudi Arabia

[c]Department of Molecular Science and Engineering, National Taipei University of Technology, No. 1, 5 Section 3, Chung-Hsiao East Road, Taipei 106, Taiwan, Republic of China

† Electronic supplementary information (ESI) available. See DOI: https://doi.org/10.1039/d4ta06264g

‡ These authors contributed equally.

chemical stability, phase purity, corrosion resistance under electrochemical conditions, and ability to serve as active sites.[11–14] The vulnerability of the material plays a key role in tuning the electronic properties out of which TMCs have a high tendency to involve d-orbitals, while main group metals and metalloids primarily involve s- and p-orbitals. Also, the hybridization of TMCs occurs when the d-orbitals of the metal hybridize with the s- and p-orbitals of the carbon atoms, broadening the d-band. This hybridization endows TMCs with properties similar to those of precious metals, such as facilitating electron transfer.[15–17] Thus, TMCs are a class of materials with many properties including electrical conductivity, chemical stability, and electronic structures, which make them useful for energy storage and electrocatalysis. The d-orbitals of TMCS can exhibit vibrant adsorption towards enriched d-electrons as they are the adsorbents present in the d-orbital. Transition metals can form TMCs by incorporating carbon sources.[18] In this process, the sp-hybridized state of transition metals is transferred to the central surface to hybridize with the d- and s-states of carbon atoms. This interaction leads to an excess of occupied orbitals, providing a greater number of electrons to π-orbitals. This process results in similar crystalline structures for all TMCs, with carbon atoms of similar size locatedin the interstitial space of the transition metals. TMCs exhibit higher stability towards carbonization and hydrocarbon isomerization than Pt-group metals. This enhanced stability can be attributed to alterations in the carbon atom configuration, leading to an increase in the metal–metal distance.[19,20] Consequently, this results in a constriction of the d-band and an increase in the density of states at the Fermi level. TMCs commonly exhibit a cubic crystal structure[18] and can be synthesized through a range of methods, such as chemical vapor deposition, solid-state reactions, and powder metallurgy techniques.[21–23] Since there are concerns regarding the stability and sustainability of TMCs synthesized through these methods, we pursue a facile synthesis approach for TMCs delivering a tailored carbon content based on the crystal structure and microstructure, achieved through a thermochemical synthesis process (Scheme 1).

This study demonstrated a facile synthesis procedure for different TMCs, including titanium carbide (TiC), vanadium carbide (VC), molybdenum carbide (MoC), and tungsten carbide (WC). The structural, crystalline, and morphological studies of the prepared different TMCs were performed using X-ray diffraction (XRD) analysis with Rietveld refinement, Raman spectroscopy and X-ray photoelectron spectroscopy (XPS) analysis, which proved that the synthesized TMCs consisted of only single phases. The electrocatalytic activity of as-synthesized TMCs was further investigated for the HER and OER to understand their energy levels by varying the symmetric and asymmetric thermodynamic free-energy landscapes.[24] VC and MoC among the prepared TMCs are close to Pt and Ir on the primary volcano plot and as expected, showed higher activity compared to that of other TMCs.[25] Specifically, the synthesized WC showing a Pt-like electronic structure exhibited excellent HER activity with the lowest overpotential of 295 mV @ 100 mA cm^{-2} and a Tafel slope of 45 mV dec^{-1}. Also, MoC presented superior

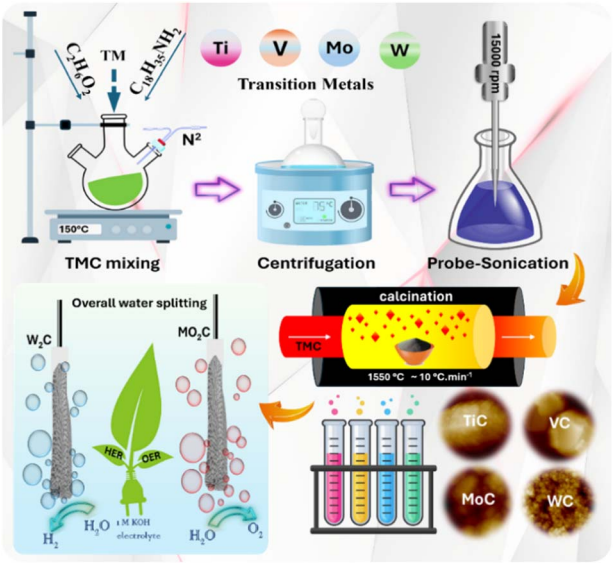

Scheme 1 Overall schematic illustration for preparing transition metal carbides (TMCs) for overall water splitting.

OER activity with an overpotential of 373 mV @ 100 mA cm^{-2} and a Tafel slope of 33 mV dec^{-1}. The density functional theory (DFT) calculations with the mechanistic approach on the TMC surfaces suggested that the (200) planes of WC and MoC were demonstrated to be involved in the redox process with a positive correlation between their activity and oxidation states. Additionally, the sustained morphology and oxidation states observed for WC and MoC during the long scanning time strongly supported their viability as commercial alternatives in various electrocatalyst applications.

Results and discussion

X-ray diffraction phase analysis of TMCs

The synthesized TMC samples were analyzed through X-ray diffraction spectroscopy to study the structural and phase

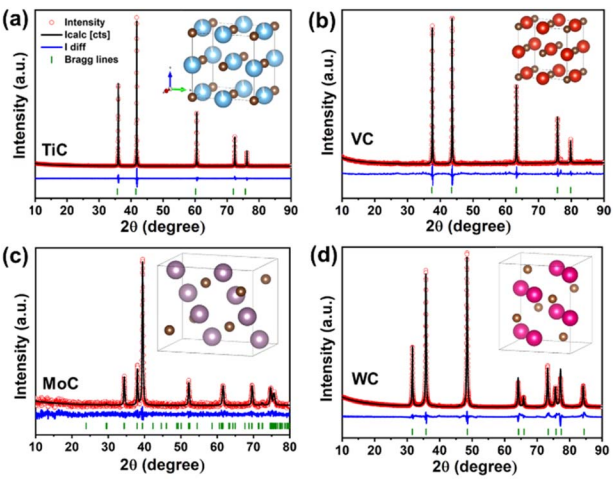

Fig. 1 XRD patterns plotted with Rietveld refinement analysis of TMCs with respective crystal structures; (a) TiC, (b) VC, (c) MoC, and (d) WC.

constitution through Rietveld refinement analysis and the results are displayed in Fig. 1. The distinct peaks at 2θ values between 36 and 42° are detected for all synthesized TMCs without any impurities in diffraction patterns. These peaks correspond to the characteristic peaks of metal–carbon sources of face-centered cubic (fcc)-M, suggesting that single phase TMCs are synthesized. Specifically, the TiC in Fig. 1a belongs to halite and crystallizes in a cubic $Fm\bar{3}m$ space group (#225) with lattice parameters a, b, c (Å) = 4.327 Å, α, β, γ = 90.00° and a unit cell volume of 81.059 Å^{x3}. Here Ti^{4+} is bound to six equivalent C^{4-} atoms forming a mixture of edge and corner-sharing TiC_6 octahedral structures where the Ti–C bond length is 2.19 Å. Simultaneously, C^{4-} is again bound to six equivalent Ti^{4+} atoms forming another edge and corner-sharing CTi_6 octahedron with the Wyckoff 1a position belonging to the Ti^{4+} species of the octahedra with positions (x, y, z) of Ti 4a (0, 0, 0) and C 4b (0, 0, $\frac{1}{2}$). The crystal structure of TiC is shown in the inset of Fig. 1a. The observed 2θ peak positions and their planes are 35.94° (111), 41.86° (020), 60.92° (022), 72.33° (131), and 76.38° (222), corresponding to TiC (ICDD-98-061-8927). Similarly, the prepared VC also belongs to a halite group and crystallizes in a cubic $Fm\bar{3}m$ space group (#225) with lattice parameters a, b, c (Å) = 4.164 Å, α, β, γ = 90.00° and a unit cell volume of 72.219 Å^{x3} (Fig. 1b). V^{4+} is bound to six C^{4-} equivalent atoms forming a mixture of edge and corner sharing VC_6 octahedra with a V–C bond length of 2.09 Å. The C^{4-} is bound to six V^{4+} equivalent atoms forming a CV_6 octahedron with a Wyckoff 1a position belonging to the V^{4+} species of the octahedra with positions (x, y, z) of V 4a (0, 0, 0) and C 4b (1/2, 0, 0). The crystal structure of VC is shown in the inset of Fig. 1b. The detected 2θ peak positions and planes are 37.73° (111), 43.67° (020), 63.26° (022), 75.91° (131), and 79.74° (222) corresponding to VC (ICDD-98-061-9056). MoC belongs to the vanadium nitride-like structure crystallizing in an orthorhombic *Pbcn* space group (#60) with lattice parameters a (Å) = 4.733 Å, b (Å) = 6.35 Å, c (Å) = 5.203 Å, α, β, γ = 90.00° and a unit cell volume of 148.686 Å^{x3} (Fig. 1c). Here, Mo^{2+} forms a distorted T-shape geometry with three equivalent C^{4-} atoms with two shorter (2.09 Å) and one longer (2.14 Å) Mo–C bond lengths. Simultaneously, C^{4-} atoms are bound to six equivalent Mo^{2+} (8d) atoms forming a corner and edge-sharing CMo_6 octahedron with a slight change in its angle from ~49 to 51°. The Wyckoff positions belong to Mo^{2+} species of the trigonal plane with positions (x, y, z) of Mo 8d (0.24, 0.07, 0.877) and C 4c (1/2, $\frac{3}{4}$, 0.876) respectively. The crystal structure of MoC is shown in the inset of Fig. 1c. The major 2θ peak positions and planes observed are 34.34° (021), 38.12° (200), 39.29° (121), 52.04° (221), 61.48° (132), 69.74° (302), 74.23° (240), and 75.64° (104) corresponding to Mo_2C (ICDD-98-006-5701). WC belongs to the beta form of the vanadium nitride-like structure crystallizing in an orthorhombic *Pbcn* space group (#60) with lattice parameters a (Å) = 4.75 Å, b (Å) = 5.23 Å, c (Å) = 6.11 Å, α, β, γ = 90.00° and a unit cell volume of 152.22 Å^{x3} (Fig. 1d). The crystal structure and phase identities were similar to those of the MoC sample with W^{2+} in a distorted T-shaped geometry with three C^{4-} atoms aligning with two shorter (2.13 Å) and one longer (2.15 Å) W–C bonds forming a CW_6 octahedral shape. The Wyckoff positions belong to W^{2+} (8d) species of the trigonal plane with positions (x, y, z) of W 8d (0.245, 0.0813, 0.124) and C 4c (1/2, $\frac{3}{4}$, 0.1214) respectively. The crystal structure of WC is shown in the inset of Fig. 1d. The major 2θ peak positions and planes observed are 31.63° (001), 35.81° (200), 48.42° (101), 64.16° (110), 65.82° (002), 73.21° (111), 75.61° (20-2), 77.16° (102), and 84.17° (201) corresponding to W_2C (ICDD-98-026-0166). To understand the effect of metal on carbide lattice parameters, the Wyckoff position, bond angle, bond length, crystallite size, and strain results obtained from Rietveld refinement for TMCs are summarized and compared in Table S1.† The crystal structures of TMCs are drawn using VESTA and mercury software. It is evident from the Rietveld fits that the prepared TiC has a similar structure and valence state variations to VC, and MoC behaves similarly to WC, which suggests that MoC and WC might display high electrical conductivity with similar material characteristics, and TiC and VC might exhibit similar oxidative and free electron vacant positions.[13] In order to further understand the crystalline quality and degree of materials, the obtained diffraction peaks of synthesized TMCs were modelled using the pseudo-Voigt function which is a convolution of Gaussian profile and Lorentzian profile functions,[26]

$$I(2\theta) = I_0 + A\left[m_u\frac{2}{\pi}\frac{w}{4\left[(2\theta)-(2\theta)_c\right]^2 + wc + (1-m_u)\frac{\sqrt{4\log 2}}{\sqrt{\pi w}}\exp\left[\frac{4\log 2}{[w]^2}\left[(2\theta)-(2\theta)_c\right]\right.}\right]$$

where $(2\theta)_c$ is the peak position, w is the distribution width, m_u is the Lorentzian parameter contributing to the peak shape, and the other terms are standard parameters. The Williamson–Hall method is employed to compute the average crystallite size and intrinsic strain TiC-6774 (56) Å, 0.0233 (1)%; VC-547 (2) Å, 0.001 (1)%; MoC-8.74 (4) Å, 0.4 (1)%; WC-268.25 (3) Å, 0.3391 (4)%.

Raman spectroscopy

Raman spectroscopy is employed to understand the behavioral patterns of variations in chemical and polymorphic structures for the prepared TMCs. Fig. 2 displays the Raman spectra for the obtained TMCs which can be deconvoluted using Briet–Wigner–Fano (BWF) line shapes in combination with multiple

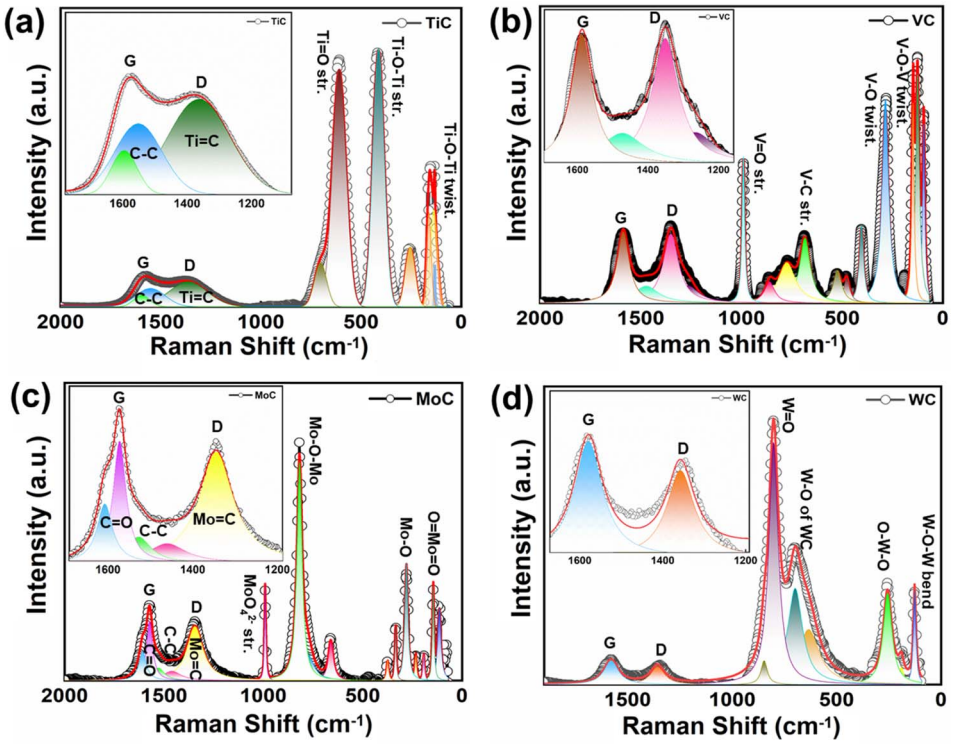

Fig. 2 Deconvoluted Raman spectra of TMCs using multiple Lorentzian and BFW functions; (a) TiC, (b) VC, (c) MoC, and (d) WC.

Lorentzian peak functions which is a suitable fitting method for the asymmetric peaks to obtain ideal and accurate peak bonding positions.[26] According to the Ferrari and Robertson model,[27] the deconvolution of the main D- and G-bands for the prepared TMCs gives a good fit to carbon sources in a broad energy range (Note S2† provides details on the conditions used for Raman spectroscopy analysis and fitting). All TMCs displayed metal–carbon based Raman peaks with two distinct phonon models contributing to the Raman scattering with a C-line shape of the G-band, revealing a high-frequency shoulder, and the D-band which shows the defect-induced band characteristic of the microcrystalline graphite system. Fig. 2a displays deconvoluted Raman peaks for TiC where the characteristic D- and G-bands of carbon appear at 1360 and 1581 cm^{-1} (sub-1551 and 1597 cm^{-1}), respectively, with a clear intensity for the disordered sp^3-hybridized carbon bonded modifications with a planar size of 2.5 to 3 nm and an I_G/I_D intensity ratio of 1.162. Upon oxidation the bands at 133, 156, and 252 cm^{-1} can be assigned to Ti–O–Ti deformation twisting, the band at 410 cm^{-1} corresponds to Ti–O–Ti stretching, and the peak at 608 (sub-704) cm^{-1} is assigned to Ti=O stretching in TiO_3. The deconvoluted Raman spectra of VC in Fig. 2b show carbon bands at 1356 cm^{-1} for the D-band with the G-band peaks at sub-1249, and 1477 cm^{-1} owing to V–C and C=C and 1591 cm^{-1} with an I_G/I_D intensity ratio of 1.173 and a planar size of 2.6 to 3.1 nm, which is consistent with the sp^3-hybridization. The scattering bands at 95, 125, 145, and 282 cm^{-1} correspond to the V–O–V bending vibrational modes of the VO^3 ion, and the bands at 404, 478, and 521 cm^{-1} correspond to V–O twisting, while the band at 691 cm^{-1} is attributed to V–C stretching, which is shared with the corner-shared oxygen of CV_6 vibrational stretching of VO_3^{2-} ions. The bands at 775, 861, and 991 cm^{-1} correspond to the V=O stretching of the VoO_3 octahedral atom. The deconvoluted Raman spectra of MoC (Mo_2C phase) in Fig. 2c exhibit the carbon characteristic bands at 1346 cm^{-1} for the D-band, sub-1458 cm^{-1} for Mo–C and 1573 cm^{-1} for the G-band with sub −1530, 1572, and 1608 cm^{-1} owing to Mo=C, C=O, and C–C with an I_G/I_D variation of 1.172 and a planar size of 2.8 to 3.4 nm. The scattering bands due to the presence of vibrational MoO_4^{2-} ions are observed between 111 and 1000 cm^{-1}. Also, the bands at 111, 145, 192, 233, and 279 cm^{-1} are observed for O=Mo=O twisting deformation, and the bands at 334 and 374 cm^{-1} are for Mo=O bending vibrations. The bands at 662, and 821 (775) cm^{-1} correspond to Mo–O–Mo stretching and breaking of Mo_2–O bonds at corner-shared oxygen atoms, and 992 cm^{-1} is observed for Mo=O stretching occurring in MoO_4^{2-} ions.[28] Fig. 2d displays the deconvoluted Raman spectra of WC with sp^2-hybridized carbon atoms at 1364 (D-band) and 1584 cm^{-1} (G-band) with an I_G/I_D intensity ratio of 1.16 and a planar size of 2.9 to 3.3 nm. The bands appearing at 127 (small peak), 192, and 256 cm^{-1} correspond to W–O–W bending vibrations where 256 cm^{-1} is due to O–W–O deformation, 693 cm^{-1} (sub-633 and 698 cm^{-1}) corresponds to W–O and 797 cm^{-1} (sub-878 cm^{-1}) corresponds to W=O, attributed to the stretching mode O–W–O of the WC phase.[11] Overall, the Raman study for the synthesized TMCs shows a similar I_G/I_D intensity ratio with differences in Raman spectra which are only due to the changes in bond ordering, not their sp^2/sp^3 hybridization. Thus, MoC and WC are considered efficient carbide sources due to their dislocation density

variations at the lateral edges and their sp^2-hybridization phenomena. The interplay of dislocation density variations and sp^2-hybridization in carbides is central to optimizing their efficiency. Low dislocation densities contribute to mechanical integrity, while sp^2 hybridization enhances electronic and thermal properties. This synergy makes carbides versatile and high performing in applications ranging from industrial tools to energy storage and electronics. Furthermore, Raman depth profiling was performed for the synthesized TMCs to investigate the absorption coefficient, refractive index, and influence of ions on the epitaxial layer.[14] The distribution of Raman signal with respect to the depth direction (along the *z*-axis) with multilayers and their 2D elemental mapping obtained from depth profiling are shown in Fig. S1 and S2,† respectively. The variation in phonon line intensity of A_{1g} (S) and E_g (S) with respect to the focus of the depth beneath the surface was observed, where the intensity of the phonon line gradually decreased as the depth focus moved to the inner part of the sample. Although the E_2H mode signal for MoC and WC has increased, it is evident that the depth scan of all TMCs remains roughly the same without any variations in the interatomic potentials, indicating a homogeneous distribution of the carbide phase with minimal variations in chemical bonding.

X-ray photoelectron spectroscopy

The chemical states and chemical compositions of the prepared TMCs were studied through X-ray photoelectron spectroscopy (XPS) which provides the minimum energy required to eject the outer electrons of individual atoms, *i.e.*, binding energy (BE) and the individual atomic contents. The peaks of individual atoms obtained from the XPS survey spectra of TMCs were further fitted to obtain the precise oxidation states and involved bonds. Furthermore, the XPS depth profile spectra were investigated to obtain elemental compositions at different layers of the carbides to understand the mechanism of carbide layer formation. As shown in Fig. S3a,† the XPS survey spectra of TiC showed peaks at 455.6, 283.9, and 528 eV for Ti 2p, C 1s and O 1s at the surface, respectively. In the high resolution Ti 2p spectra of TiC (Fig. S6a†), two sets of doublets were observed where the doublet for Ti^{4+} 2p–C was split into Ti^{4+} 3/2 and Ti^{4+} 1/2 with a separation of 4.5 eV and the spin coupled Ti^{4+} 3/2 and 1/2 were separated by 5.58 eV.[29,30] The high resolution C 1s spectra of TiC were fitted to C–Ti, C–C, C=C, C–O, and C=O (Fig. S6b†). Also, the oxygen associated with Ti and C in the crystal structure corresponds to the peaks at 528.09 and 529.89 eV (Fig. S6c†). Fig. S6d–f† illustrate the XPS depth profile spectra of TiC with 10 depth variations for Ti, C, and O elements. It is evident that no change or shift in peaks has been observed, suggesting that the prepared TiC structure is stable. The V 2p, C 1s, and O 1s peaks appeared in the survey spectra of VC as shown in Fig. S3b,† and the high-resolution spectra for elements of VC and their individual states were further fitted as shown in Fig. S7a–c.† The wide peaks between 515 and 525 eV for V 2p were fitted to obtain doublets for +4 and +5 oxidation states of V 2p with the separation of 7.08 and 7.47 eV, respectively.[31,32] The C 1s peak appeared at 283.7 eV, corresponding to C–V, C–C, C=C, C–O, and C=O bonds. The associated O 1s peaks around 530 eV were further fitted to obtain peaks for V–O, C–O, and O–H. Fig. S7d–f† illustrate the XPS depth profile spectra with 10 depth variations for V, C, and O. No noticeable change or shift in peaks was observed, indicating the stable VC structure. Similarly, the survey scan for synthesized MoC exhibits the Mo 3d, Mo 3p C 1s, and O 1s peaks (Fig. S3c†). In the high resolution Mo 3d spectra of MoC in Fig. 3a, the Mo 3d peak at 233 eV in the broad XPS spectra was further analyzed to obtain the

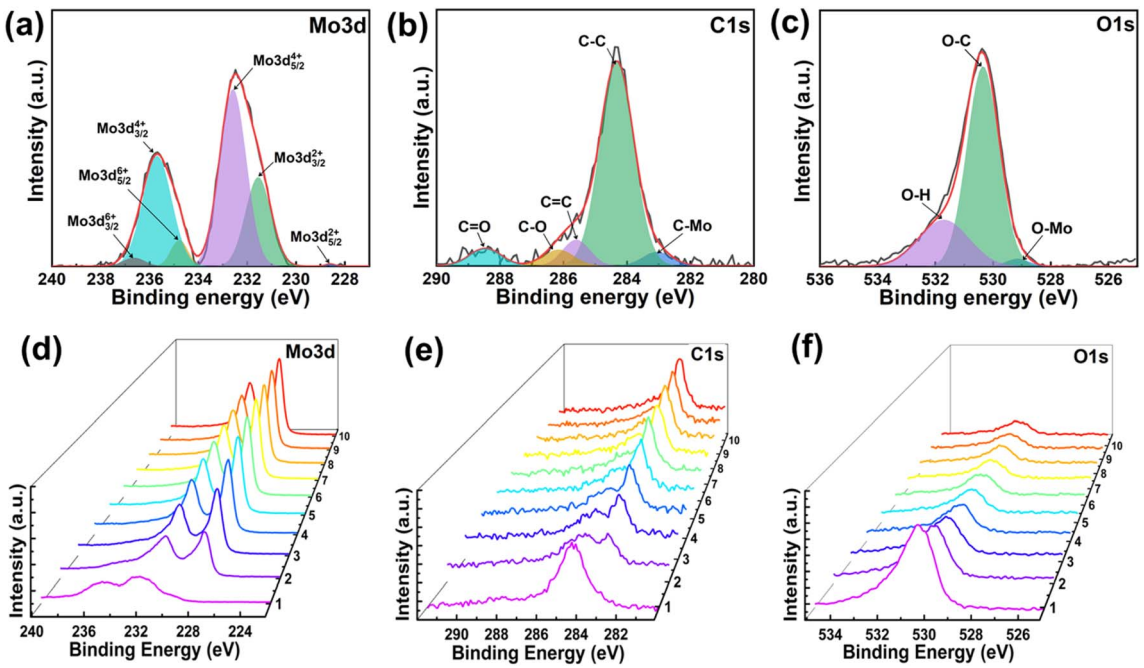

Fig. 3 High resolution XPS spectra and depth profile spectra for individual elements of MoC; (a and d) Mo 3d, (b and e) C 1s, and (c and f) O 1s.

spin–orbit coupled +2, +4, and +6 oxidation states of Mo 3d with the corresponding doublets (5/2 and 7/2) separated by 2.96, 3.11, and 2.0 eV, respectively.[33,34] This multi-valency of Mo 3d can be attributed to the variation in the nucleation rate at specific reaction sites and abundant d-electrons. The corresponding high resolution C 1s peak at 284 eV was deconvoluted into C–Mo, C–C, C=C, C–O, and C=O bonds (Fig. 3b). The O 1s peak in MoC also can be depicted as Mo–O, O–C, and O–H bonds with the C–O peak as the highest intense peak over 531 eV (Fig. 3c). Furthermore, the XPS depth profile spectra were recorded with 10 depth variations for Mo, C, and O elements of MoC where no change in peak or shift along the depth was observed, which indicates that the synthesized MoC has a stable structure.

The survey scan of the prepared WC in Fig. S3d† displays the presence of W 4f, W 4d, W 4p, C 1s, and O 1s peaks, and the W 4f, C 1s, and O 1s peaks in WC at 31.1, 283.9, and 529.0 eV were further analyzed individually (Fig. 4a–c). The W 4f peak was fitted to W $4f^{4+}$–C, W $4f^{4+}$ and W^{6+} doublets with a separation of 2.6, 2.8, and 2.0 eV, respectively.[35,36] The C 1s peak was also fitted to C–W, C–C, C=C, C–O, and C=O peaks while the O 1s peak was fitted to O–W, O–C, and O–H. Fig. 4d–f show the XPS depth profile spectra with 10 depth variations for W, C, and O elements in the prepared WC. The stable peaks along the depth were observed for all elements, showing that WC with a stable structure was synthesized. In addition, the XPS depth profiling survey spectra with the atomic ratio of each element for the prepared TMCs remain unaltered in the original metal peak with the increase in etching time, evidencing the stability of the synthesized TMCs (Fig. S4 and S5†). The presence of surface O 1s for all synthesized TMCs is observed, although aerial oxidation was prevented in the synthesis process to avoid forming the interstitial O atoms within the M–C lattice structure irrespective of surface termination. However, the partial oxidation at the surface of TMCs could not be avoided at room temperature, but it can facilitate the Brønsted acid site promoted electrocatalysis.[11] The surface oxidation helped to introduce the C/O heterojunction that further boosted the electrocatalytic activity through introducing defect induced active sites and modifying the electronic states. The variation in atomic % of the O element and M–O/M–C bond ratio in TMCs is ascribed to different degrees of interactions. The details of peak positions and corresponding peak areas as well as the full width at half maximum (FWHM) in the XPS results are summarized in Table S2.† Also, the atomic % values of individual elements as obtained from XPS analysis are listed in Table S3.† The higher content of C–O and O–H bonds than M–O bonds indicated higher surface hydroxylation and chemisorption of oxygen due to the oxophilicity of the material surface over interstitial oxygen atoms within the MO lattice. The nature of TMCs with zero oxidation states was predominant as metals (M) interact peripherally with carbon atoms by descending from the stabilized ligands. This electronic state of TMCs can be understood through the mechanistic steps of TMC formation. Fig. S8 and Note S3† demonstrate the proposed formation scheme of TMCs and the justification of the oxidation state towards XPS depth profiling.[37]

Morphological studies

Morphological analysis of the prepared TMC samples was carried out using field-emission scanning electron microscopy (FE-SEM) combined with energy-dispersive X-ray spectroscopy (EDS). The FESEM images of the TiC nanocluster reveal that the synthesized TiC has a nanoplate structure with sub-micrometer size. This TiC nanocluster with distorted agglomeration is

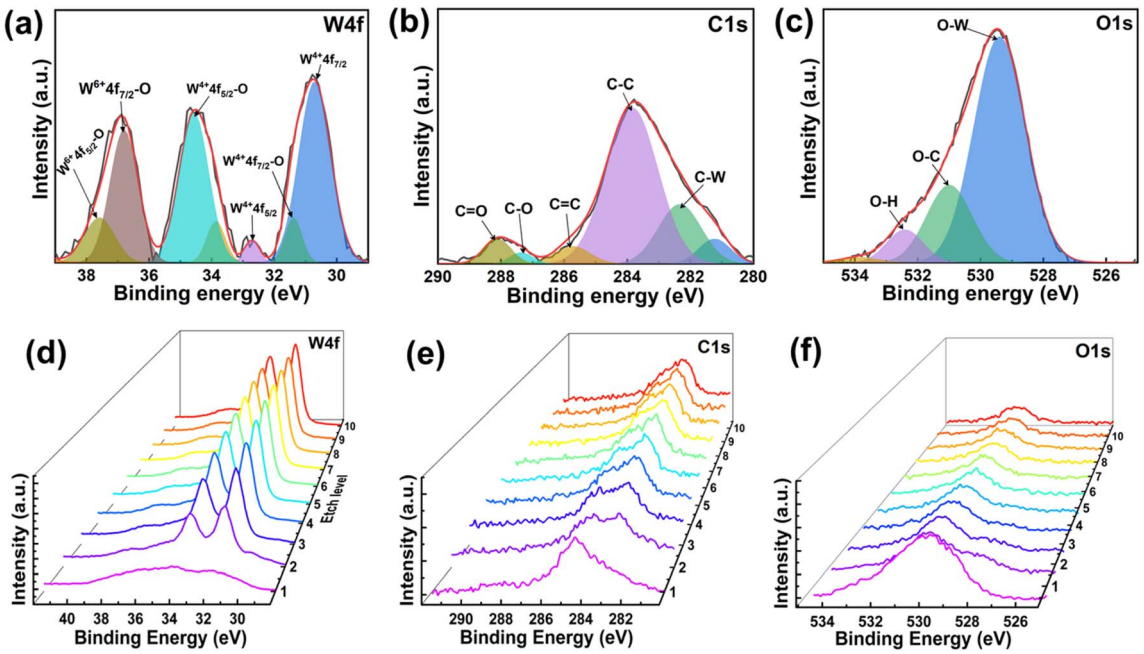

Fig. 4 High resolution XPS spectra and depth profile spectra for individual elements of WC; (a and d) W 4f, (b and e) C 1s, and (c and f) O 1s.

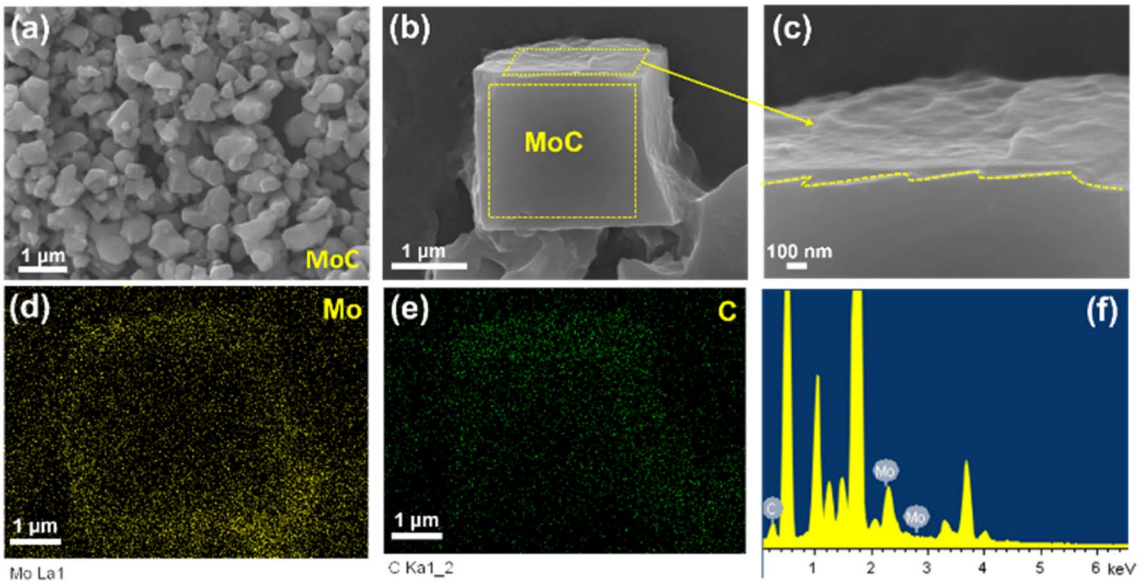

Fig. 5 FE-SEM morphological analysis: (a–c) MoC nanostructure and (d–f) elemental mapping of Mo and C elements with the EDX spectrum.

observed because of the metal interaction with carbon during the carbonization process. The elemental mapping image of TiC with the EDX spectrum shows the uniform distribution of Ti and C elements (Fig. S9†). The FESEM images for VC exhibit the microstructure of conglomerates with a random cuboidal shape in the nano-range and the EDS analysis reveals the uniform presence of V and C in the prepared VC (Fig. S10†). The FESEM images in Fig. 5a–c reveal a cubical morphology for MoC with agglomeration at the micro level where the cube surface displays a layered carbon structure with Mo in its center. Fig. 5d–f show the elemental mapping of Mo and C elements with the EDX mapping spectrum supporting the occupancy of Mo and C. The FESEM images in Fig. 6a–c show a nano-mixture of WC crystalline nanoparticles surrounded by ultrathin shells which are further confirmed by HR-TEM images (Fig. S11†). The elemental mapping with the EDX spectrum for WC nanoparticles shows the uniform presence of W and C elements (Fig. 6d–f). The synthesized TMCs display a distorted and irregular structure which is due to the combination of metal and carbon sources through high temperature carbonization. However, these structures did not affect their crystalline parameters or structure and all synthesized TMCs show a single phase without any impurities.

Electrocatalytic analysis

The electrocatalytic activity of the synthesized TMCs was studied for overall water splitting. The electrocatalytic measurements were carried out using a typical three-electrode system. The TMC catalyst slurry was coated on nickel foam

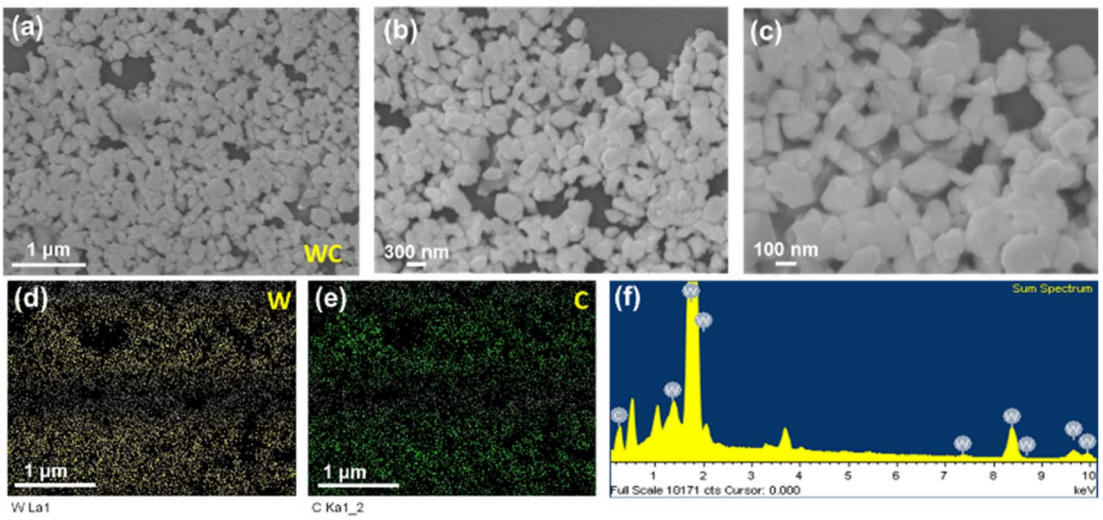

Fig. 6 FE-SEM morphological analysis: (a–c) WC nanostructure and (d–f) elemental mapping of W and C elements with the EDX spectrum.

and was used as the working electrode (WE). A graphite rod and a Hg/HgO electrode were used as the counter electrode (CE) and the reference electrode (RE), respectively. The RE was calibrated to obtain the electrode potential of 0.927 V. All potentials for redox reactions were presented with respect to the reversible hydrogen electrode (RHE) potential with *iR* correction. The MoC and WC catalysts coated on the nickel foam were characterized with the XPS depth profile to investigate the degradation of TMCs after the electrocatalytic measurements (Fig. S12 and S13†). Detailed discussion on the post-scanning electronic states of the materials is provided in the following section. In the HER electrocatalytic measurement, WC exhibits the lowest overpotentials and higher current densities indicating its superior activity among the synthesized TMCs (Fig. 7a). Although the exchange current density (J_0) from the intercept at the equilibrium potential of VC was slightly higher than that of WC, the WC electrode demonstrated high current density with the lowest overpotential in the long run (0.25, 0.09, 0.08, 0.08, and 0.15 mA cm^{-2} for TiC, VC, MoC, WC, and Pt/C, respectively). The overpotential at the current density 100 mA cm^{-2} (η_{100}) of WC (295 mV) was comparable to that of commercial Pt/C (287 mV) with a consistent increase in the current densities dependent on overpotential (Fig. S14a–c†).[38] The progress of the reaction and the rate determining step was further analyzed through the Tafel slope (*b*-coefficient) obtained from the lower and higher overpotential over log |*J*| values. The calculated *b*-coefficient of WC in a lower overpotential region showed the lowest value of 45 mV dec^{-1} among the prepared TMCs (Fig. 7b), which is close to that of the Heyrovsky step ($M - H + H_2O + e^- \rightarrow M + OH^- + H_2$, $b = 40$ mV dec^{-1}) for desorption for all materials. Additionally, the calculated *b*-coefficient of WC in a higher overpotential region was the lowest value of 172 mV dec^{-1} among the synthesized TMCs (Fig. S14d†) which is higher than that of the Volmer adsorption step ($M + H_2O + e^- \rightarrow M - H + OH^-$, $b = 120$ mV dec^{-1}), indicating the fact that most active sites are occupied, increasing the surface coverage with the progress of the reaction[39] and the adsorption step at this state becomes the slowest step to be considered as the rate determining step. For the TMCs, the M–C hybridization might lead to the higher electron density of the states at the Fermi level and a broader unoccupied d-band, leading to better coverage of adsorbed H on the surface boosted by larger active sites. This also stands as a moderating factor for the Volmer step to be predominant in higher overpotential regions.[40,41] The HER mechanism is further understood from XRD patterns of the post-HER for the TMCs. In the HER process, it has been seen

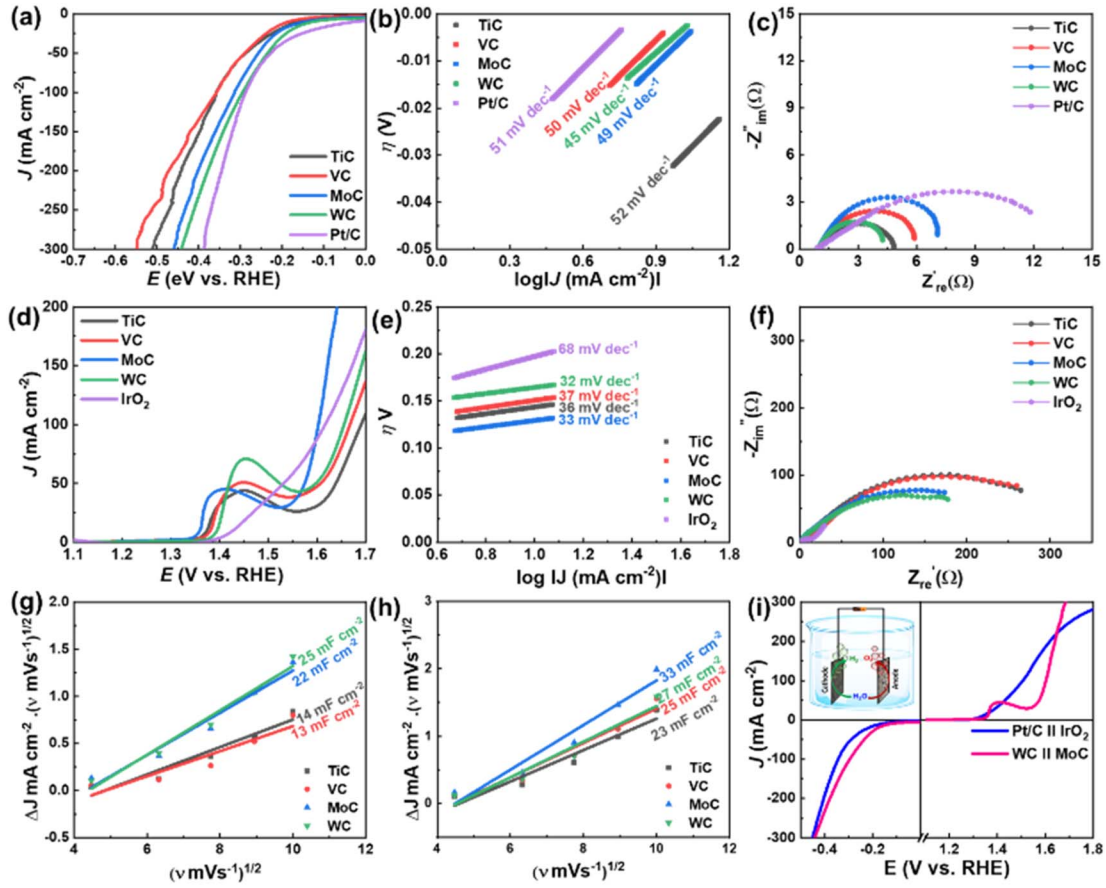

Fig. 7 (a) The polarization curves of TMCs, (b) their Tafel slopes in the lower overpotential region, and (c) the Nyquist plots for the HER. (d) Polarization curves of TMCs, (e) their Tafel slopes in the lower overpotential region, and (f) the Nyquist plots for the OER. (g and h) Relative current density *vs.* (scan rate)$^{1/2}$ plots of TMCs for the calculation of C_{dl} for the HER and OER. (i) The polarization curves of the overall water electrolysis system using WC||MoC electrodes (inset: schematic illustration).

that the adsorption of H* intermediates does not directly depend on the metal atoms in the cluster, but rather on the carbide atom termination.[42] The post-HER XRD patterns in Fig. S14e and S17† showed a slight variation in peak intensities and positions of TMCs other than WC, indicating instability as the carbide layer at the surface and superiority of WC for the HER during this long time where the WC surface retains most of its electronic properties. Furthermore, the modification in the (200) plane intensity/position might be due to the C–H bond formation. The proposed reaction path has been confirmed through theoretical modelling which shows the lowest free energy for carbide termination. A detailed discussion on DFT calculations along with the mechanistic path with respect to the density of states (DOS) of the carbides has been discussed in the following section and Note S4 and S5.† Moreover, WC possesses a similar band structure near the Fermi level to the top edge of the occupied level of Pt which would leverage the electrocatalytic behavior of WC, similar to that of Pt with the lowest reaction free energy, close to zero. The efficiency of the catalysts was further revealed through the turnover frequency (TOF) values which indicated the average number of products per unit site. WC possesses the highest TOF value of 0.075 s^{-1} at 200 mV among different TMCs (Table S4 and Fig. S14f†). These values are well supported by the electrochemically active surface area[43] (ECSA) (ECSA = C_{dl}/C_s, detailed calculations in the ESI†) values, calculated in the non-faradaic region of 0.2 to 0.1 V *vs.* RHE as seen in Fig. 7g. The electrochemical impedance spectroscopy (EIS) measurements were further performed to study the charge transfer kinetics. The charge transfer resistance (R_{ct}) values of TMC catalysts for the HER were measured from the diameter of the semicircle Nyquist plot obtained from the EIS measurement. The obtained R_{ct} values for the TMCs were small enough, indicating smooth progress of the reaction on the TMC surfaces, and WC showed the lowest value of 1.66 Ω (Fig. 7c), indicating that WC has low charge transfer resistance as well as fast charge transfer for the HER. As shown in Table S4,† this excellent electrocatalytic activity of WC toward the HER outperforms that of previously reported electrocatalysts. Moreover, the long-term stability of the WC catalyst toward the HER was further studied using the chronoamperometric tests for 60 h of continuous operation at a constant applied voltage of 170 mV. As shown in Fig. S15a,† the WC catalyst delivered superior stability with 92% retention of the initial current density over 60 h. In addition, the XPS analysis after the HER cycle test showed that WC retained its oxidation states over long-time scanning with the proportional change in individual bonds due to the interaction with intermediates and delocalization of electron densities (Fig. S15b–d†). The C–W bond shows noticeable change after long-time scanning due to the C atom dependent H* adsorption on the surface, while the intensities of oxygen species improved to maintain the charge balance and also the W 4f peaks shifted to slightly higher BE regions to accommodate the electron transfer process of proton reduction.[44] The stabilities of other TMCs were also tested with respect to the potential and the results show that the TMCs exhibit good stability over 60 h (Fig. S15e†).

Furthermore, the prepared TMCs were explored for the electrolytic activities toward the OER. The OER polarization curves of TMCs in Fig. 7d showed that MoC among the as-synthesized TMCs achieves the highest current density at lower overpotential with a minimum overpotential η_{100} of 373 mV which is comparable to that of the commercial IrO_2 catalyst (380 mV). At a certain potential, MoC delivered higher current densities with respect to both the electrode surface area and ECSA, calculated for the OER in the non-faradaic potential range of 0.7 to 0.9 V *vs.* RHE (Fig. S16a–c†). It is interesting to observe such activity as electroactive sites generally determine the actual area on which the electrochemical reaction of interest occurs;[45] again it should be kept in mind that the redox reaction here consists of adsorption and desorption of reaction intermediates that primarily depend on the binding energy between the catalyst element (M or M–X, X = O, C, OH) and the intermediates (here O-intermediates) which are generated during the four steps involving water adsorption, dissociation into OH, association of another H_2O and formation of OOH and finally dissociation of OOH into O_2. From the point of electronegativity and exposed facets for reactions (elaborated discussion during DFT studies), the better activity of MoC for the OER can be understood, satisfying the Sabatier principle. Moreover, the ECSA trend for the OER was different from that of the HER following another factor that the double layer capacitance (C_{dl}) depended on the ion association over the electrolyte–electrode double layer that is more favoured over Mo–C than W–C for anions.[46] The capacitance at the double layer depended on the electrode surface and its ability to accommodate intermediates. The formed OH_{ad}–$M^+(H_2O)_x$ or $(H_2O)_{x-1}M^+\cdots H_2O\cdots OH_{ad}$ clusters attach to the electric double layer by the noncovalent bond and hence Mo–C; Mo having partially filled d orbitals provided better activity than WC, where W has constrained d-orbitals for the OER. The reaction kinetics of TMCs towards the OER was further investigated from the Tafel slopes and R_{ct} values. The Tafel slopes of TMCs were calculated in lower and higher overpotential regions as shown in Fig. 7e and S16d,† respectively. The *b*-coefficient for all TMCs increased with the increase of log |*J*|.[47] As calculated from the Tafel plot, the Tafel slopes were determined to be 36, 37, 32, 33, and 68 mV dec^{-1} in the lower overpotential region. Since the Tafel slope values are too close, the exchange current density (J_0) values were considered to justify the activity of TMCs. The obtained J_0 values from the extrapolation of the Tafel slopes are 1.2×10^{-3}, 1.23×10^{-3}, 1.48×10^{-3}, 1.02×10^{-3}, and 1.58×10^{-3} mA cm^{-2} for TiC, VC, MoC, VC, and IrO_2, respectively. It shows the superior OER activity of the MoC catalyst with the highest J_0 value among the as-synthesized TMCs. Now, the calculated Tafel slopes of the TMCs indicate that the reaction rate follows unity in the lower overpotential region according to the Butler–Volmer kinetics model and its rate determining step can be the second step of the overall reaction.[48] The lower value of Tafel slopes indicates stronger adsorption of the intermediates in the primary adsorption step, following the equation,[48]

$$b = \frac{2.303\ RT}{F\alpha}, \quad \alpha = \frac{n_f}{\gamma} + n_r\beta$$

where n_f and n_r are the number of electrons transferred before and after each occurrence of the RDS, γ is the stoichiometric number, generally 1, and β is the symmetrical potential barrier. However, the increase in the Tafel slope values in the higher overpotential region can be attributed to the higher surface coverage with the increase in the reaction time and overpotential.[39] The XRD analysis of MoC after the OER measurement showed a change in the peak position and intensity of the (200) phase at 41.17°, indicating the adsorption of OH* molecules on the MoC surface (Fig. S16e†). It can be realized that the Brønsted acid sites in the MoC catalyst were created by the presence of terminal oxygen atoms in the M–C lattice, specifically on 4f and 5d metals with higher oxidation states and higher electrophilicity, which can facilitate the adsorption of oxygenated intermediates during the progress of the reaction. The reaction path and the involved energy barrier have further been discussed through the DFT calculations in the following section (Note S4 and S5†). The reaction kinetics of TMCs were further studied through EIS measurement and Fig. 7f shows their Nyquist plots. The calculated R_{ct} values were determined to be 169.6, 202.7, 132.0, and 122.5 Ω for TiC, VC, MoC, and WC, respectively. It can be seen that the R_{ct} results are in agreement with the Tafel slope results in the lower overpotential region, which is related to the small perturbation of the potentials.[49] The R_{ct} values of TMCs for the OER are quite higher than those for the HER, indicating the sluggish anodic reaction involving four electrons.[50] Interestingly, although MoC exhibited higher R_{ct} (132.0 Ω) than WC (122.5 Ω), the MoC catalyst delivered higher O_2 production, which is supported by the highest TOF value of 0.043 s^{-1} @ 400 mV (Fig. S16f†), suggesting the fact that R_{ct} is not a crucial factor for the OER. In addition, it can be seen in Table S5† that these excellent OER activities of the MoC catalyst outperform that of the previously reported electrocatalysts. The stability and durability of the MoC catalyst were evaluated using the chronoamperometric tests over 60 h of continuous operation at a constant applied voltage of 1.3 V. The results exhibit a negligible change in current density for MoC during the cycling test, where almost 99% of the initial current density was retained (Fig. S17a†). The excellent stability of the MoC catalyst was further explored by XPS analysis after the cycling test (Fig. S17b–d†). The XPS results after the cycling test demonstrate almost unaltered peak positions for each element in the survey scan, indicating good stability of oxidation states in MoC. However, the change in the intensity and FWHM of individual bonds in Mo 3d and C 1s clearly presents the interaction of MoC with the intermediates of the OER which is consistent with the post-OER XRD study. Compared to the chronoamperometric tests for other TMCs of TiC, VC, and WC, MoC demonstrated better cycle stability for the long term OER (Fig. S17e†). Furthermore, the comparative XRD study for the synthesized TMCs before and after the electrocatalytic reaction suggests that a similar mechanistic path occurs on the carbide surfaces, however, the electronic environment and the position of energy bands with respect to the Fermi level caused the modification of the catalyst-adsorbate bond strength for facile kinetics (Fig. S18†). Moreover, the XPS depth profile results of the post-HER for WC and post-OER for MoC showed that the surface oxidation states were only affected after the reaction, indicating surface involved redox reactions (Fig. S19 and S20†). The surface M–C and M–O centers only adsorbed the water dissociated into H* or OH*/OOH*/O* with no atoms from the next layer of bulk hosting these intermediates due to atomic constraints and the structural barrier, resulting in unaltered bulk oxidation states. The C/O heterojunction caused alterations to the band structure of the central metal atom that caused a direct electron transfer process assisted by the single electron proton coupled electron transfer process for the OER.

The mechanistic pathway for the redox reaction was further investigated through the oxygen reduction reaction (ORR) which follows the reverse mechanistic steps of the OER when the ORR undergoes a four-electron pathway (Fig. S21a†).[51] A three electrode system was constructed using individual MoC and WC coated GCEs as the working electrode, a graphite rod as the counter electrode, and a Hg/HgO electrode as the reference electrode in O_2 saturated 0.1 M KOH solution with a rotation speed range of 400 to 2400 rpm (Fig. S22a and b†). The corresponding Koutecky–Levich plots (Note S1, Fig. S22c and d†) at different potentials exhibited linearity, indicating first-order reaction kinetics for the ORR. Moreover, slopes being consistent at various potentials, the electron transfer numbers (η) were found to be the same at different potentials and the value of η was calculated to be ~3.8 indicating that the ORR is a 4-electron process. However, the polarization curve nature is yet to be explained. Fig. S21b† shows the ORR polarization curves of MoC and WC at a rotating speed of 1600 rpm and a scanning rate of 5 mV s^{-1}, where the kinetically controlled initial part of the LSV curve showed an exponential increase in current densities with decreasing potential. From the polarization curves the onset potentials (E_{onset}, indicating the initiation of electrochemical conversion) were calculated to be 0.97 V and 0.82 V whereas the half-wave potentials ($E_{1/2}$, monitoring the progress of the reaction in the kinetic-diffusion region) were calculated to be 0.83 and 0.61 V, respectively for MoC and WC, respectively. A higher positive value indicates a facile electrochemical reduction of oxygen on the MoC surface with respect to WC. This phenomenon was correlated with the Mo–O interaction as it was observed for the OER. As the reaction steps involve O_2 adsorption on the catalyst surface, its dissociation to form O, the association of O with H_2O to form OOH, and dissociation from the catalyst surface in the form of water, the Cat–O bond formation as well as breaking should be balanced according to the Sabatier Principle. Tafel slope values (Fig. S21c†) were then calculated where the lower value for MoC showed its higher activity due to facile electron transfer over the Mo–C–O network facing a lower charge transfer resistance of 2023 Ω (Fig. S21d†). The stability and methanol crossover effect on the working electrode are important factors for the fuel cell cathode where the ORR occurs as the counter reaction to fuel oxidation; the chronoamperometric studies were performed using MoC and WC. After 12 h, it was observed that MoC successfully restored balance in current output over WC implying its resistance against methanol toxicity (Fig. S22e†) establishing superior bifunctional OER and ORR activity of MoC (Fig. S22f†).

The aforementioned electrocatalytic activity studies on TMCs highlight the excellent HER activity of WC and the multifunctional activity of MoC for the OER and ORR. This behavior of WC and MoC can also be attributed to their larger C_{dl} and ECSA values which help to accommodate a greater number of substrates on the surface (Fig. 7g, h and Table S6†). The C_{dl} values of WC and MoC, calculated from the relative current density *vs.* the square root of the scan rate plot, are found to be higher for both half-cell reactions over the other two carbides respectively. From these excellent electrocatalytic activities of TMCs, a two-electrode system using WC and MoC as the cathode and anode was further investigated for overall water splitting (Fig. 7i, inset). The polarization curves of the WC||MoC electrode system delivered a cell voltage of 1.89 V to attain a current density of 100 mA cm^{-2} (Fig. 7i), which is a much lower potential compared to that of the commercial Pt/C||IrO_2 electrode system (2.08 V). In addition, it can be observed that vigorous H_2 and O_2 gas bubbles are generated from the prepared WC and MoC electrodes during overall water splitting, respectively (ESI Video†). The comparison of cell voltages of the recently reported catalysts is provided in Table. S7,† and it demonstrates the impressive activities of the as-synthesized WC||MoC electrode system, which can be efficient alternatives for the traditional electrocatalysts for the hydrogen-based energy industry.

Density functional theory study

From the above experimental results, it is evident that WC and MoC appeared as superior cathode and anode materials for the electrocatalytic HER and OER among the synthesized TMCs. The theoretical understanding of the electrochemical activities of WC and MoC was achieved using DFT computations (Note S4† provides details on the DFT calculations, PDOS and the band structure of MoC and WC with the results in Fig. S23a and b†). During the atomic modeling, the W_2C (200) and Mo_2C (200) planes were chosen as the reactive sites of WC and MoC catalysts, respectively, and the free energy diagrams were calculated on the (200) planes of the respective materials at $U = 0$ V *vs.* RHE (Fig. 8a). The choice of the (200) plane was made as itwas prominently observed at the surface from the lattice fringe and SAED pattern in the HR-TEM study (Fig. S11†) and this plane for both MoC and WC was found to be affected after post-scanning XRD patterns. Moreover, the HER and OER activities for W_2C (200) and Mo_2C (200) were compared simultaneously to better understand their activity as cathode and anode materials in a two-electrode system. In the water splitting process, H_2O molecules are adsorbed and dissociated on the active site of the catalyst. The (200) plane of the catalyst was taken as the active site for the adsorption and dissociation of H* or O*/OOH*/OH* intermediates to form H_2 and O_2, respectively. We calculated the activation barriers for the dissociation of water over both the surfaces using the CI-NEB method as shown in Fig. S24.† The activation barriers for water dissociation are 1.28 and 2.49 eV over W_2C and Mo_2C surfaces, respectively. Also, water dissociation is an endothermic process with 0.92 and 1.03 eV over W_2C and Mo_2C surfaces, respectively. The Gibbs free energy of the adsorbed hydrogen (ΔG_{H^*}) for the HER was calculated using the following equation where the catalyst having ΔG_{H^*} close to zero is considered to be a highly efficient catalyst.[52,53]

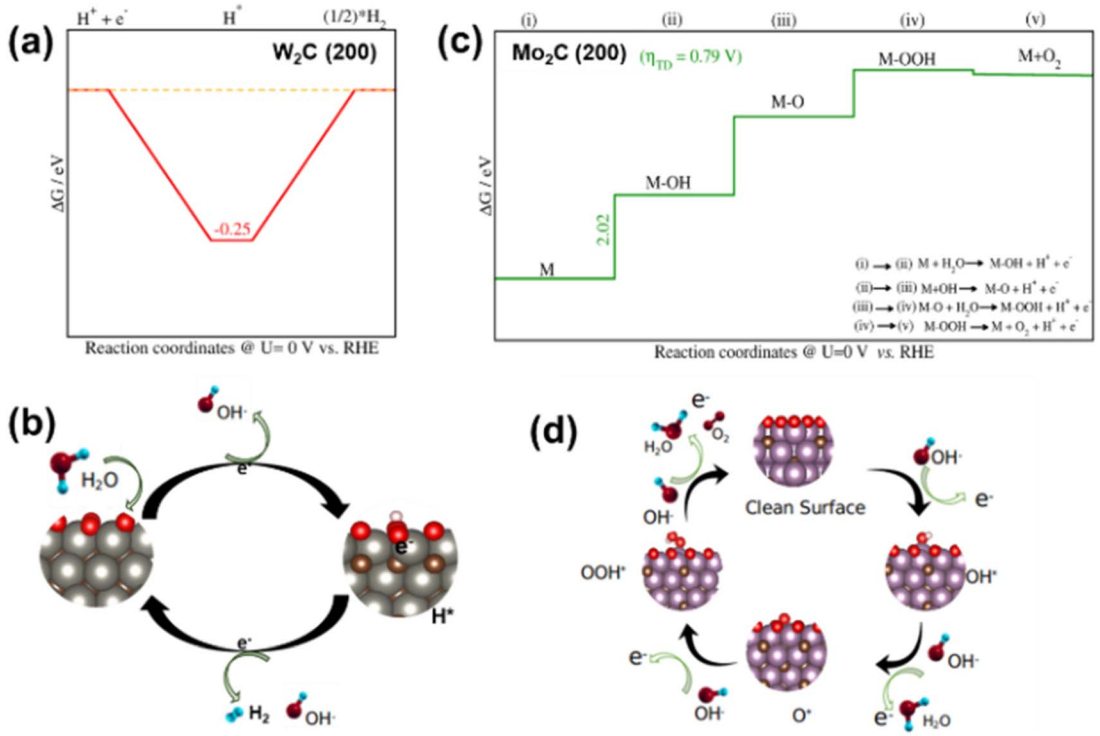

Fig. 8 (a) HER energy profile diagram and (b) the reaction progress scheme on the W_2C (200) surface. (c) OER energy profile diagram and (d) the reaction progress scheme on the Mo_2C (200) surface.

The chemisorption energy (ΔE_{H^*}) for the adsorbed hydrogen is taken from our computations. ΔE_{ZPE} is the difference between the zero-point energy of the adsorbed hydrogen and the gas phase hydrogen and $T\Delta S_H$ is the entropy correction for the adsorbed hydrogen at $T = 298.15$ K, which are 0.035 eV and −0.205 eV, respectively. The ΔG_{H^*} values for W_2C (200) and Mo_2C (200) were obtained as −0.25 eV and −0.37 eV, respectively. ΔG_H of the commercial Pt catalyst was observed to be −0.09 eV. It is yet to achieve the optimal catalytic activity with a free energy value of $\Delta G_H = 0$, inferring the role of thermodynamic stability and loss of catalytic performance due to strong binding between hydrogen and the catalyst surface.[54] The present calculations show that WC would perform as a cathode material for the HER with lower ΔG_{H^*} values. The progress of the reaction can be understood from the position of the intermediate (H*) on the WC catalyst surface as shown in Fig. 8b. In addition, the OER process contains multiple steps unlike the HER which makes the overall process sluggish as multiple energy barriers are to be conquered during the progress of the reaction. To understand the performance of the HER, we have plotted the projected density of states of H adsorbed Mo_2C and W_2C systems as shown in Fig. S25.† In the case of the Mo_2C system, a significant peak corresponding to the 1s orbital of hydrogen hybridized with the 2p orbital of oxygen can be observed at −9.56 eV, in comparison to −9.23 eV in the case of W_2C. PDOS analysis signifies the weaker adsorption of H over W_2C when compared with Mo_2C. To understand the performance of the OER, we have plotted the PDOS of OH adsorbed Mo_2C and W_2C systems as shown in Fig. S26.† In the case of the Mo_2C system, a significant peak corresponding to the 1s orbital of H hybridized with the 2p orbital of O and 3d orbital of Mo can be observed at −7.55 eV. In contrast, this significant peak is observed at −8.44 eV in the case of the W_2C system. The upshift in the H 1s and O 2p states indicates the stronger covalent interactions with W 3d states in the W_2C system.[1] This signifies the stronger adsorption of OH over W_2C which leads to a higher overpotential for the OER when compared to Mo_2C. The Gibbs free energy of H_2O adsorption has been calculated to be −0.04 eV, and −0.007 eV for W_2C (200) and Mo_2C (200), respectively, showing stable adsorption of H_2O over W_2C (200) which is essential to expedite the OER process.[55] The overall Gibbs free energy is calculated comprising the ΔG_n, ($n = 1$–n, n = number of steps) of each reaction step involved in the OER.[56–59] The ΔG_n ($n = 1$–4) values for Mo_2C were 2.02, 3.93, 5.06, and 4.92 eV, whereas these values for W_2C were 1.43, 0.87, 4.98, and 4.92 eV with OOH intermediate formation being the slowest step. Fig. 8c shows that all OER steps are exothermic, and step 4 ($OOH^* \rightarrow O_2$) for Mo_2C (200) is exothermic, whereas the large Pt catalyst step being associated with the OH* step. The thermodynamic overpotential (η_{TD}) is obtained as 0.79 V which is necessary to make all the reaction steps exothermic.[58,60] However, step 2 ($OH^* \rightarrow O^*$) for W_2C (200) had an exothermic nature and the η_{TD}

$$\Delta G_{H^*} = \Delta E_{H^*} + \Delta E_{ZPE} - T\Delta S_H$$

was calculated to be 2.67 V for the facile progress of the reaction although the longest step was the association of OOH*. The favorable active sites for O* intermediates on Mo_2C (200) and W_2C (200) were found to be the bridge site (M–O bond) and the hollow site, respectively, while that for the OH*/OOH* intermediates were found to be on top of the metal atom as shown in the schematic cycle of the OER (Fig. 8d) (Note S5† provides details on the water splitting mechanism). The lower value of η_{TD} for Mo_2C (200) revealed that the Mo_2C has superior OER activity compared to W_2C (200). In the HER process, W_2C (200) exhibits higher activity than Mo_2C (200). Hence, the DFT investigations (Fig. S27–S29†) are consistent with the above experimental results, suggesting that WC and MoC would be excellent electrocatalytic electrodes for the HER and OER in overall water splitting, respectively.

Conclusion

Different TMCs were prepared through a facile carbonization process with a fixed-bed reactor with the structure of TMCs depending on the type and concentration of the carbon source. The XRD-Rietveld refinement and Raman–Lorentzian peak fitting showed that the prepared TMCs are synthesized in a single phase without any impurities which is also confirmed by the XPS depth profiling study. The electronic properties of the TMCs were well-suited for electrocatalytic water splitting. The prepared WC and MoC among the TMCs showed excellent electrocatalytic activities toward the HER and OER with lowest overpotentials of 295 and 373 mV at a current density of 100 mA cm^{-2} with excellent stability, respectively. The synthesized WC and MoC are further applied as cathode and anode materials in the overall water splitting cell system, and they delivered excellent electrocatalytic performance with a cell voltage of 1.89 V at a current density of 100 mA cm^{-2}. Furthermore, the DFT studies showed that the thermodynamic overpotentials of the OER for the prepared WC and MoC were 2.67 and 0.79 V, respectively, and the Gibbs free energies of the HER for them were 0.25 and 0.37 eV. These results support the experimental results showing the superior HER and OER electrocatalytic activities of WC and MoC, respectively. These results suggest that the prepared TMCs can be potential alternatives to novel metal based electrocatalysts for energy conversion applications.

Experimental section

Chemicals

All chemicals and reagents unless specified were purchased from Sigma-Aldrich. The source chemicals for transition metals used here are titanium hexacarbonyl, vanadium hexacarbonyl, molybdenum hexacarbonyl, and tungsten hexacarbonyl. All chemicals used were of AR grade with 99% purity and were used as received unless specified; no modifications were performed. Double-distilled water (DDW) was used throughout the experiments.

Synthesis of TMCs

For the synthesis of TMCs, a mixture solution of ethylene glycol ($C_2H_6O_2$, 20 mL) and oleylamine ($C_{18}H_{35}NH_2$, 10 mL) in a three-neck flask was purged with nitrogen for 30 min at room

temperature. Then, 500 mg of titanium hexacarbonyl (or other transition metal source chemicals for preparing different TMCs) was added into the mixture solution under a nitrogen atmosphere with vigorous stirring for 12 h at 150 °C. After cooling down to room temperature, the obtained solution was washed with ethanol and water, and then centrifuged at 15 000 rpm for 30 min. The precipitate was collected and dried in a vacuum oven for 12 h at 80 °C. The obtained powder was transferred to a clean fused alumina boat and put into the furnace. The powder sample was then heated at a constant heating rate (10 °C min^{-1}) to the desired temperature (1450–1550 °C) and the reduction process was allowed to continue for a definite period. A continuous purified argon flow of 100 mL min^{-1} was maintained throughout the whole thermal cycle. Subsequently, the product sample was rapidly cooled and flushed with purified argon to avoid the oxidation of the product sample. After cooling down to room temperature, the product sample was collected and kept in a desiccator for further characterization.

Computational details

All the DFT calculations were completed using the Vienna *ab initio* simulation package (VASP).[61,62] We utilized the generalized gradient approximation (GGA)–Perdew–Burke–Ernzerhof (PBE)[63] and the projector augmented wave (PAW) method with an energy cutoff of 520 (400) eV for bulk (slab) structures.[64] A Γ-centered fine k-spacing of 0.02 (0.03) × 2π/Å was used for bulk (slab) calculations.[65] All atoms in the bulk (slab) geometry were relaxed until the net forces on each atom reached <0.001 (0.02) eV $Å^{-1}$. The self-consistent-field electronic energies were converged to a precision of 1×10^{-8} (1×10^{-4}) eV for bulk (slab). The optimized lattice constants, which are $a/b/c$ = 4.74/6.06/5.23 Å for Mo_2C and $a/b/c$ = 4.74/5.22/6.09 Å for W_2C, were found to be consistent with our experimentally observed lattice parameters with the error of less than 0.5% for each dimension for both the compounds. The experimentally observed (200) surface in this study was used to cleave the surface for the systems used in this study. The DFT-D3 type van der Waals (VdW) dispersion correction and dipole corrections were included for all the slab geometry optimization.[66] A total of eleven alternative metal-carbon layers were used for the computation, with the bottom six fixed layers. A vacuum of 15 Å was used for the slab. The structural models for Mo_2C (200) and W_2C (200) with different adsorbates are already displayed in Fig. 1 (inset). The (200) surface for both the systems was stabilized by decorating the surface with an oxygen monolayer.[67] Crystal structures were visualized using VESTA software.[68]

Details of characterization studies and electrocatalytic measurements are given in the ESI.†

Data availability

Data supporting the findings of this study have been included as part of the ESI† and additional data are available from the corresponding authors upon reasonable request.

Author contributions

T. S. K. S. and J. J. contributed equally to the work. T. S. K. S.: investigation, formal analysis, writing – original draft, writing – review & editing. J. J.: investigation, formal analysis, writing original draft, revision. B. M. B.: investigation, formal analysis. M. A. G.: review & editing. K. C. B. and K. S. S. V. P. R: DFT studies. K.-Y. H.: writing – review & editing. S. G. K.: software. J. S. C.: funding acquisition. S. H. H.: writing – review & editing. W. M. C.: conceptualization, funding acquisition, supervision, writing – review & editing.

Conflicts of interest

There are no conflicts to declare.

Acknowledgements

This work was supported by the Core Research Institute Basic Science Research Program (2021R1A6A1A03038858) and the Regional Leading Research Center Program (No. RS-2023-00217778) through the National Research Foundation of Korea (NRF), funded by the Korean government (MIST). The authors thank the Researchers Supporting Program (RSP2025R518) funded by King Saud University.

References

1 T. Liu, P. Li, N. Yao, G. Cheng, S. Chen, W. Luo and Y. Yin, *Angew. Chem., Int. Ed.*, 2019, **58**, 4679–4684.
2 D. Voiry, M. Chhowalla, Y. Gogotsi, N. A. Kotov, Y. Li, R. M. Penner, R. E. Schaak and P. S. Weiss, *ACS Nano*, 2018, **12**, 9635–9638.
3 J. Jana, T. S. K. Sharma, B. M. Babu, N.-D. Huynh, J. S. Chung, W. M. Choi and S. H. Hur, *Int. J. Hydrogen Energy*, 2024, **77**, 1276–1285.
4 F. Dionigi, Z. Zeng, I. Sinev, T. Merzdorf, S. Deshpande, M. B. Lopez, S. Kunze, I. Zegkinoglou, H. Sarodnik, D. Fan, A. Bergmann, J. Drnec, J. F. de Araujo, M. Gliech, D. Teschner, J. Zhu, W. X. Li, J. Greeley, B. R. Cuenya and P. Strasser, *Nat. Commun.*, 2020, **11**, 1–10.
5 H. Jin, C. Guo, X. Liu, J. Liu, A. Vasileff, Y. Jiao, Y. Zheng and S.-Z. Qiao, *Chem. Rev.*, 2018, **118**, 6337–6408.
6 X. Peng, C. Pi, X. Zhang, S. Li, K. Huo and P. K. Chu, *Sustainable Energy Fuels*, 2019, **3**, 366–381.
7 S. A. Zahra, M. Waqas Hakim, M. Adil Mansoor and S. Rizwan, *Electrochim. Acta*, 2022, **434**, 141257.
8 S. Kogularasu, Y. Lee, B. Sriram, S. Wang, M. George, G. Chang-Chien and J. Sheu, *Angew. Chem., Int. Ed.*, 2024, **63**, e202311806.
9 C.-L. Su, K. Sakthivel, Y.-T. Yao, P.-H. Liao, M.-L. Lee and J.-K. Sheu, *ACS Appl. Energy Mater.*, 2021, **4**, 8030–8035.
10 S. Kogularasu, B. Sriram, S.-F. Wang and J.-K. Sheu, *ACS Sustain. Chem. Eng.*, 2022, **10**, 15115–15123.
11 M. A. R. Anjum, M. H. Lee and J. S. Lee, *ACS Catal.*, 2018, **8**, 8296–8305.

12 L. Liao, X. Bian, J. Xiao, B. Liu, M. D. Scanlon and H. H. Girault, *Phys. Chem. Chem. Phys.*, 2014, **16**, 10088–10094.
13 Y.-J. Ko, J.-M. Cho, I. Kim, D. S. Jeong, K.-S. Lee, J.-K. Park, Y.-J. Baik, H.-J. Choi and W.-S. Lee, *Appl. Catal., B*, 2017, **203**, 684–691.
14 S. Meyer, A. V. Nikiforov, I. M. Petrushina, K. Köhler, E. Christensen, J. O. Jensen and N. J. Bjerrum, *Int. J. Hydrogen Energy*, 2015, **40**, 2905–2911.
15 M. S. A. Sher Shah, G. Y. Jang, K. Zhang and J. H. Park, *EcoEnergy*, 2023, **1**, 344–374.
16 D. B. Kumar, W. Nie, Z. Jiang, J. Lee and T. Maiyalagan, *J. Alloys Compd.*, 2023, **960**, 170828.
17 X. Liu, P. Wang, X. Liang, Q. Zhang, Z. Wang, Y. Liu, Z. Zheng, Y. Dai and B. Huang, *Mater. Today Energy*, 2020, **18**, 100524.
18 J. Jana, T. S. K. Sharma, J. S. Chung, W. M. Choi and S. H. Hur, *J. Alloys Compd.*, 2023, **946**, 169395.
19 Y. Deng, Y. Ge, M. Xu, Q. Yu, D. Xiao, S. Yao and D. Ma, *Acc. Chem. Res.*, 2019, **52**, 3372–3383.
20 M. Ying, R. Tang, S. Zhao, W. Yang, W. Liang, X. Zhang, G. Yang, R. Zheng, H. Pan, X. Liao and J. Huang, *Adv. Energy Sustainability Res.*, 2021, **2**, 1–8.
21 H. Bin Wu, B. Y. Xia, L. Yu, X. Y. Yu and X. W. Lou, *Nat. Commun.*, 2015, **6**, 1–8.
22 Z. W. Seh, K. D. Fredrickson, B. Anasori, J. Kibsgaard, A. L. Strickler, M. R. Lukatskaya, Y. Gogotsi, T. F. Jaramillo and A. Vojvodic, *ACS Energy Lett.*, 2016, **1**, 589–594.
23 B. Qin, Y. Li, Q. Zhang, G. Yang, H. Liang and F. Peng, *Nano Energy*, 2020, **68**, 104374.
24 K. S. Exner, *Mater. Today Energy*, 2021, **21**, 100831.
25 K. S. Exner, *Acc. Chem. Res.*, 2024, **57**, 1336–1345.
26 T. Sanjay Kanna Sharma, J. Jana, K. C. Bhamu, J. Song, S. Sivaselvam, T. Van Tam, S. G. Kang, J. S. Chung, S. H. Hur and W. M. Choi, *Chem. Eng. J.*, 2023, **464**, 142673.
27 A. C. Ferrari and J. Robertson, *Philos. Trans. R. Soc. London, Ser. A*, 2004, **362**, 2477–2512.
28 Y. Wang, B. Kong, D. Zhao, H. Wang and C. Selomulya, *Nano Today*, 2017, **15**, 26–55.
29 A. Ignaszak, C. Song, W. Zhu, J. Zhang, A. Bauer, R. Baker, V. Neburchilov, S. Ye and S. Campbell, *Electrochim. Acta*, 2012, **69**, 397–405.
30 A. A. Galuska, J. C. Uht and N. Marquez, *J. Vac. Sci. Technol., A*, 1988, **6**, 110–122.
31 X. Peng, L. Hu, L. Wang, X. Zhang, J. Fu, K. Huo, L. Y. S. Lee, K. Y. Wong and P. K. Chu, *Nano Energy*, 2016, **26**, 603–609.
32 J. Yu, X. Gao, G. Chen and X. Yuan, *Int. J. Hydrogen Energy*, 2016, **41**, 4150–4158.
33 D. Wang, J. Wang, X. Luo, Z. Wu and L. Ye, *ACS Sustain. Chem. Eng.*, 2018, **6**, 983–990.
34 J. Jiang, Q. Liu, C. Zeng and L. Ai, *J. Mater. Chem. A*, 2017, **5**, 16929–16935.
35 K. T. Ng and D. M. Hercules, *J. Phys. Chem.*, 1976, **80**, 2094–2102.
36 L. Qiao, A. Zhu, W. Zeng, R. Dong, P. Tan, Z. Ding, P. Gao, S. Wang and J. Pan, *J. Mater. Chem. A*, 2020, **8**, 2453–2462.
37 J. Quinson and K. M. Ø. Jensen, *Adv. Colloid Interface Sci.*, 2020, **286**, 102300.
38 J. D. Gojgić, A. M. Petričević, T. Rauscher, C. I. Bernäcker, T. Weißgärber, L. Pavko, R. Vasilić, M. N. Krstajić Pajić and V. D. Jović, *Appl. Catal., A*, 2023, **663**, 119312.
39 T. Shinagawa, A. T. Garcia-Esparza and K. Takanabe, *Sci. Rep.*, 2015, **5**, 13801.
40 M. Miao, J. Pan, T. He, Y. Yan, B. Y. Xia and X. Wang, *Chem.–Eur. J.*, 2017, **23**, 10947–10961.
41 N. Mahmood, Y. Yao, J. W. Zhang, L. Pan, X. Zhang and J. J. Zou, *Adv. Sci.*, 2018, **5**(2), 1700464.
42 M. Ďurovič, J. Hnát and K. Bouzek, *J. Power Sources*, 2021, **493**, 229708.
43 C. M. Schott, P. M. Schneider, K.-T. Song, H. Yu, R. Götz, F. Haimerl, E. Gubanova, J. Zhou, T. O. Schmidt, Q. Zhang, V. Alexandrov and A. S. Bandarenka, *Chem. Rev.*, 2024, **124**, 12391–12462.
44 S. Roy, D. Bagchi, L. Dheer, S. C. Sarma, V. Rajaji, C. Narayana, U. V. Waghmare and S. C. Peter, *Appl. Catal., B*, 2021, **298**, 120560.
45 J. Jana, T. Van Phuc, J. S. Chung, W. M. Choi and S. H. Hur, *Nanomaterials*, 2022, **12**, 4348.
46 C. M. Schott, P. M. Schneider, K. T. Song, H. Yu, R. Götz, F. Haimerl, E. Gubanova, J. Zhou, T. O. Schmidt, Q. Zhang, V. Alexandrov and A. S. Bandarenka, *Chem. Rev.*, 2024, **124**(22), 12391–12462.
47 A. Govind Rajan and E. A. Carter, *Energy Environ. Sci.*, 2020, **13**, 4962–4976.
48 L. Negahdar, F. Zeng, S. Palkovits, C. Broicher and R. Palkovits, *ChemElectroChem*, 2019, **6**, 5588–5595.
49 K. Park, B.-Y. Chang and S. Hwang, *ACS Omega*, 2019, **4**, 19307–19313.
50 Y. P. Sánchez, A. Santos and P. R. Bueno, *J. Phys. Chem. C*, 2022, **126**, 3151–3162.
51 M. Chen, J. Liu, W. Zhou, J. Lin and Z. Shen, *Sci. Rep.*, 2015, **5**, 1–10.
52 W. A. Saidi, *J. Phys. Chem. Lett.*, 2013, **4**, 4160–4165.
53 S. Sinthika, U. V. Waghmare and R. Thapa, *Small*, 2018, **14**, 1703609.
54 S. Prabhakaran and D. H. Kim, *Appl. Surf. Sci.*, 2023, **614**, 156255.
55 X. Huang, J. Wang, J. Gao, Z. Zhang, L.-Y. Gan and H. Xu, *ACS Appl. Mater. Interfaces*, 2021, **13**, 17075–17084.
56 M. T. M. Koper, *J. Electroanal. Chem.*, 2011, **660**, 254–260.
57 J. Rossmeisl, Z.-W. Qu, H. Zhu, G.-J. Kroes and J. K. Nørskov, *J. Electroanal. Chem.*, 2007, **607**, 83–89.
58 I. C. Man, H. Su, F. Calle-Vallejo, H. A. Hansen, J. I. Martínez, N. G. Inoglu, J. Kitchin, T. F. Jaramillo, J. K. Nørskov and J. Rossmeisl, *ChemCatChem*, 2011, **3**, 1159–1165.
59 Q. Liang, G. Brocks and A. Bieberle-Hütter, *JPhys Energy*, 2021, **3**, 026001.
60 K. S. Exner, *ChemCatChem*, 2021, **13**, 4066–4074.
61 G. Kresse and J. Furthmüller, *Phys. Rev. B:Condens. Matter Mater. Phys.*, 1996, **54**, 11169–11186.
62 G. Kresse and J. Furthmüller, *Comput. Mater. Sci.*, 1996, **6**, 15–50.

63 J. P. Perdew, K. Burke and M. Ernzerhof, *Phys. Rev. Lett.*, 1996, **77**, 3865–3868.
64 P. E. Blöchl, *Phys. Rev. B:Condens. Matter Mater. Phys.*, 1994, **50**, 17953–17979.
65 H. J. Monkhorst and J. D. Pack, *Phys. Rev. B*, 1976, **13**, 5188.
66 S. Grimme, J. Antony, S. Ehrlich and H. Krieg, *J. Chem. Phys.*, 2010, **132**, 154104.
67 X. Huang, J. Wang, H. Bing Tao, H. Tian, Z. Zhang and H. Xu, *J. Catal.*, 2020, **389**, 461–467.
68 K. Momma and F. Izumi, *J. Appl. Crystallogr.*, 2011, **44**, 1272–1276.